Geosci. Model Dev. Discuss., 8, 3403–3441, 2015
www.geosci-model-dev-discuss.net/8/3403/2015/
doi:10.5194/gmdd-8-3403-2015

Geoscientific Model Development Discussions
Open Access

The Louvain-la-Neuve sea ice model LIM3.5: global and regional capabilities

C. Rousset[1], M. Vancoppenolle[1], G. Madec[1], T. Fichefet[2], S. Flavoni[1], A. Barthélemy[2], R. Benshila[3], J. Chanut[4], C. Levy[1], S. Masson[1], and F. Vivier[1]

[1]Sorbonne Universités (UPMC Paris 6), LOCEAN-IPSL, CNRS/IRD/MNHN, Paris, France
[2]Centre Georges Lemaître for Earth and Climate Research, Université catholique de Louvain, Louvain-la-Neuve, Belgium
[3]CNRS/LEGOS, Toulouse, France
[4]Mercator Ocean, Ramonville Saint-Agne, France

Received: 24 March 2015 – Accepted: 10 April 2015 – Published: 29 April 2015

Correspondence to: C. Rousset (clement.rousset@locean-ipsl.upmc.fr)

Published by Copernicus Publications on behalf of the European Geosciences Union.

Abstract

We present the new 3.5 version of the Louvain-la-Neuve sea ice model (LIM) integrated in NEMO 3.6. The main novelty is the improvement of model robustness and versatility for a wide range of applications, from global to regional scales. Several modifications to the code were required. First, the time stepping scheme of the model was changed from parallel to sequential (ice dynamics first, then thermodynamics). Such a scheme enables to diagnose the different physical processes responsible for exchanges through the air–ice–ocean interfaces, as well as the online inspection of mass, heat and salt conservation properties of the code. In the course of these developments, several minor conservation leaks were found and fixed, so that LIM3.5 is exactly conservative. Second, lateral boundary conditions for regional ice-covered configurations have been implemented. To illustrate the new capabilities, two simulations are performed. One is a global simulation at a nominal 2° resolution forced by atmospheric climatologies and is found reasonably realistic although no specific tuning was done. The other is a regional simulation at 2 km resolution around the Svalbard Archipelago in the Arctic Ocean, with prescribed conditions at the four boundaries including tides. The simulation is able to resolve small-scale features and transient events such as the opening and closing of coastal polynyas. The ice mass budgets for both simulations are illustrated and mostly differ by the strength of ice formation in open water. LIM3.5 now forms a solid base for future scientific studies and model developments.

1 Introduction

Sea ice covers 3–6 % of the Earth's surface and is characterized by ample seasonal variations, making it one of the most influential geophysical features in the Earth system (Comiso, 2010). Mostly because of its high albedo and thermal insulation power, sea ice affects the weather and more generally climate (e.g., Budkyko, 1969; Vihma, 2014). The seasonal cycle of ice growth and melt strongly impacts the vertical upper ocean

GMDD
8, 3403–3441, 2015

density structure and is a key driver of the ocean circulation at global scale through dense water formation (Aagaard and Carmack, 1989; Goosse and Fichefet, 1999). Sea ice also influences marine primary productivity and carbon export to depth (e.g. Thomas and Dieckmann, 2010; Vancoppenolle et al., 2013), and constitutes a habitat for Arctic and Antarctic fauna, including specific microbial, birds and mammal species (Croxall et al., 2002; Atkinson et al., 2004).

Given the difficulty to observe polar regions, numerical modelling is essential to understand sea ice processes and their influence on the other components of the Earth system. Indeed, a sea ice component is presently included in virtually all ocean and Earth modelling systems (e.g. Flato et al., 2013; Danabasoglu et al., 2014). The contemporary use of sea ice models encompasses a wide range of applications, from large-scale climate to small-scale process studies and operational forecasts. The physical processes at stake need to be well resolved at the appropriate spatial and temporal scales. Hence, sea ice models must be both physically reliable and versatile in a wide range of scales, and at a reasonable computational cost.

In order to match these constraints, technical changes were made to the Louvain-la-Neuve sea ice model (LIM3, Vancoppenolle et al., 2009b), leading to the version 3.5 which is presented here. LIM is the reference sea ice model in the NEMO system along with the interface for CICE (Hunke et al., 2013), and will be used in the forthcoming IPSL Earth System model (Dufresne et al., 2013), EC-Earth (Hazeleger et al., 2010), and CMCC-CM (Scoccimarro et al., 2011) CMIP6 models. For climate simulations, the exact conservation of mass, heat and salt is essential. This sanity check could not be diagnosed and was not ~~fulfilled~~ satisfied in LIM3 until now, mostly due to the time stepping scheme. Therefore, the latter was reshaped to allow the control of the exchanges at the air–ice–ocean interfaces. Several minor conservation leaks were found and corrected. Moreover, the regional capabilities of NEMO with LIM3 were limited. In particular, open boundary conditions for sea ice were not implemented which prevented regional studies in ice-covered areas. LIM3.5 is the first version which allows in and outflows communications through open boundaries.

GMDD
8, 3403–3441, 2015

This paper is organized as follows. The representation of sea ice physics in LIM is briefly described in Sect. 2. Sections 3 and 4 are dedicated to the new capabilities of LIM, which are illustrated in the framework of NEMO in its most recent version 3.6. We show how the model behaves in two configurations: (i) a large-scale global 2° resolution configuration and (ii) a regional 2 km resolution configuration around the Svalbard Archipelago, a region well suited to study various sea ice regimes as well as transient events such as polynyas. Conclusions and perspectives are presented in Sect. 5.

2 Model description

LIM was originally a B-grid sea ice model developed by Fichefet and Morales Maqueda (1997) including ice dynamics based on the viscous-plastic (VP) rheology (Hibler, 1979), the 3-layer thermodynamic formulation of Semtner (1976), the 2nd-order moment-conserving scheme of Prather (1986) and various sea ice physical parameterizations. Some years later LIM became LIM2 as it was rewritten in Fortran 90 and coupled to OPA, a C-grid, finite difference, hydrostatic, primitive equation ocean general circulation model (Madec, 2008). LIM2 was later on integrated into the NEMO system, for the global reference configuration ORCA2-LIM (Timmermann et al., 2005).

Recently, LIM was improved towards a better account of sub-grid scale physics, giving birth to LIM3 (Vancoppenolle et al., 2009a, b). New advances reside mainly in the introduction of an elastic term for rheology (EVP) on a C-grid (Bouillon et al., 2009, 2013), multiple ice categories to represent the sub-grid scale ice thickness distribution (Thorndike et al., 1975), and a multi-layer halo-thermodynamic component including brine dynamics and their impact on ice thermal properties and ice–ocean salt exchanges. A brief description of the physics of LIM is given hereafter.

GMDD
8, 3403–3441, 2015

2.1 Conservation of area and ice thickness categories

To account for unresolved sub-grid scale variations in ice thickness (h), the state of sea ice is given by a thickness distribution function $g(x, y, h, t)$ (Thorndike et al., 1975), defined as the limit

$$g = \lim_{\mathrm{d}h \to 0} \frac{\mathrm{d}A}{\mathrm{d}h}, \tag{1}$$

where $\mathrm{d}A$ is the areal fraction of a small control surface with thickness between h and $h + \mathrm{d}h$.

Invoking continuity, the conservation of area can be written as:

$$\frac{\partial g}{\partial t} = -\nabla \cdot (g\boldsymbol{u}) + \psi - \frac{\partial}{\partial h}(fg) \tag{2}$$

The terms on the right-hand side are: (i) advection by the horizontal velocity $\boldsymbol{u}$, (ii) mechanical redistribution (ψ) (i.e. ridging/rafting), and (iii) thermodynamical processes, with $f = \mathrm{d}h/\mathrm{d}t$ the net ice growth/melt rate. In practice, the thickness distribution is discretized over (typically 5) thickness categories (Bitz et al., 2001; Lipscomb, 2001), each characterized by a specific areal fraction (referred to as *concentration*). The ice thickness in each category is free to evolve between fixed boundaries.

The state of the ice is defined by a series of state variables $X(x, y, h, t, z)$, namely ice concentration, ice volume per unit area, ice internal energy, ice salt content, snow volume per unit area and snow internal energy. Ice internal energy is the only state variable which also depends on the vertical depth in the ice (z). Ice salt content does not depend on z since implicit vertical salinity profiles are assumed. Following the discretization of thickness space, state variables are characterized by specific values in each category. In addition, in order to resolve the vertical profiles of internal energy, each category is further vertically divided into one layer of snow and several ice layers of equal thicknesses.

GMDD
8, 3403–3441, 2015

In practice, sea ice state variables follow an equation of the form:

$$\frac{\partial X}{\partial t} = -\nabla \cdot (X\boldsymbol{u}) + D\nabla^2 X + \Psi^X + \Theta^X \quad (3)$$

where $\nabla \cdot (X\boldsymbol{u})$ is the horizontal advection, $D\nabla^2 X$ is the horizontal diffusion, Ψ^X is the ridging/rafting and Θ^X is the halo-thermodynamics.

2.2 Dynamics

2.2.1 Momentum equation

The ice velocity is considered the same for all categories and is determined from the two-dimensional momentum equation:

$$m\frac{\partial \boldsymbol{u}}{\partial t} = A(\tau_a + \tau_w) - mf\boldsymbol{k} \times \boldsymbol{u} - mg\nabla\eta + \nabla \cdot \sigma \quad (4)$$

where m is the ice mass per unit area, A is concentration, τ_a and τ_w are the air–ice and ocean–ice stresses, $-mf\boldsymbol{k} \times \boldsymbol{u}$ is the Coriolis force, $-mg\nabla\eta$ is the pressure force due to horizontal sea surface tilt and $\nabla \cdot \sigma$ refers to internal forces arising in response to deformation. Momentum advection is at least one order of magnitude smaller than acceleration and is neglected (Thorndike, 1986). The external stress terms are multiplied by concentration to satisfy free drift at low concentration (Connolley et al., 2004). The stress tensor σ is computed using the C-grid elastic-viscous-plastic (EVP) formulation of Bouillon et al. (2009, 2013). EVP (Hunke and Dukowicz, 1997) regularizes the original viscous-plastic (VP) approach (Hibler, 1979). VP assumes a viscous ice flow (stress proportional to deformation) at very small deformations, and a plastic ice flow (stress independent of deformation) above a plastic failure threshold. This threshold lies on a so-called charge which depends on the ice strength determined by default from Hibler (1979):

$$P = P^* \overline{H} e^{-C(1-A)} \quad (5)$$

GMDD
8, 3403–3441, 2015

where P^* and C are empirical positive parameters. $\overline{H}$ is the ice volume per grid cell area. Other strength formulations are available in the code (e.g. Rothrock, 1975; Lipscomb et al., 2007), see Vancoppenolle et al. (2012) for details. The EVP method improves accuracy at short time scales, introducing artificial damped elastic waves and a time-dependence to the stress tensor. This method enables an explicit resolution of the momentum equation with a reasonable number of sub-time steps (~ 100).

2.2.2 Horizontal transport and diffusion

The sea ice state variables are transported horizontally using the second-order moment-conserving scheme of Prather (1986). This scheme is weakly diffusive and preserves positivity of the transported ice fields. The added horizontal diffusion must be viewed as a numerical artefact to avoid non-linearities arising from the coupling between ice dynamics and transport. Horizontal diffusion is solved using a Crank–Nicholson scheme, with a prescribed diffusivity within the ice pack which drops to zero at the ice edge.

2.2.3 Ridging and rafting

The dissipation of energy associated with plastic failure under convergence and shear is accomplished by rafting (overriding of two ice plates) and ridging (breaking of an ice plate and subsequent piling of the broken ice blocks into pressure ridges). Thin ice preferentially rafts whereas thick ice preferentially ridges (Tuhkuri and Lensu, 2002). In LIM3.5, the amount of ice that rafts/ridges depends on the strain rate tensor invariants (shear and divergence) as in Flato and Hibler (1995), while the ice categories involved are determined by a participation function favoring thin ice (Lipscomb et al., 2007). The thickness of ice being deformed h' determines whether ice rafts ($h' < 0.75$ m) or ridges ($h' > 0.75$ m), following Haapala (2000). The deformed ice thickness is $2h'$ after rafting, and is distributed between $2h'$ and $2\sqrt{H^* h'}$ after ridging, where $H^* = 100$ m (Hibler, 1980). Newly ridged ice is highly porous, effectively trapping seawater. To represent

GMDD
8, 3403–3441, 2015

this process, mass, salt and heat are extracted from the ocean into a prescribed volume fraction (30 %) of newly ridged ice (Leppäranta et al., 1995). Consequently, simulated new ridges have high temperature and salinity as observed (Høyland, 2002). A fraction of snow (usually 50 %) falls into the ocean during deformation.

2.3 Halo-thermodynamics

Thermodynamics refer to the processes locally affecting the ice mass and energy, and involving energy transfers through the air–ice–ocean interfaces. Halodynamics refers to the processes impacting sea ice salinity. In the code, both processes are assumed purely vertical and their computations are repeated for each ice category. Therefore, the reference to ice categories is implicit in this section.

2.3.1 Energy

The change in the vertical temperature profile $T(z,t)$ of the snow–ice system derives from the heat diffusion equation:

$$\rho \frac{\partial E(S,T)}{\partial t} = \frac{\partial}{\partial z}\left[\kappa(S,T)\frac{\partial T}{\partial z}\right] + R \tag{6}$$

with z the vertical (layer) coordinate, ρ the snow/ice density (assumed constant), E the snow/ice internal energy per unit mass (Schmidt et al., 2004), S the salinity, κ the thermal conductivity (Pringle et al., 2007) and R the internal solar heating rate. The effect of brine inclusions are represented through the S and T dependency of E and κ (e.g. Untersteiner, 1964; Bitz and Lipscomb, 1999). The surface energy balance (flux condition) and a bottom ice temperature at the freezing point provide boundary conditions at the top and bottom interfaces, respectively. Equation (6) is non-linear and is solved iteratively. Change in ice salinity is assumed to conserve energy, hence any salt loss implies a small temperature increase.

GMDD
8, 3403–3441, 2015

The solar energy is apportioned as follows. The net solar flux penetrating through the snow–ice system is $(1-\alpha)F_{\mathrm{sol}}$, where α is the surface albedo and F_{sol} is the incoming solar radiation flux. Only a prescribed fraction i of the net solar flux penetrates below the surface and attenuates exponentially, whereas the rest is absorbed by the surface where it increases the surface temperature. The radiation term in Eq. (6) derives from the absorption of the penetrating solar radiation flux $R = -\partial/\partial z[i_0(1-\alpha)F_{\mathrm{sw}}\exp(-z/L)]$, where $L = 1\,\mathrm{m}$ is the length of attenuation. At this stage no shortwave radiation penetration is allowed when snow is present ($i_0 = 0$). The solar radiation flux penetrating down to the ice base is sent to the ocean. The surface albedo is a function of the ice surface temperature, ice thickness, snow depth and cloudiness (Shine and Henderson-Sellers, 1985).

2.3.2 Mass

The ice mass increases by (i) new ice formation in open water, (ii) congelation at the ice base, (iii) snow–ice formation at the ice surface and (iv) entrapment and freezing of seawater into newly formed ridges. And it decreases by melting at both (v) the surface and (vi) the base. The snow mass increases by snowfall and reduces by surface melting, sublimation, snow–ice formation and snow loss during ridging/rafting.

Freezing and melting (i, ii, v, vi) depend on the appropriate interfacial net energy flux (open water–atmosphere, ice–atmosphere or ice–ocean) ΔQ ($\mathrm{W\,m^{-2}}$) such that the ocean-to-ice mass flux F^{m} ($\mathrm{kg\,m^{-2}\,s^{-1}}$) is written as:

$$F^{\mathrm{m}} = \frac{\Delta Q}{\Delta E}. \tag{7}$$

ΔE ($\mathrm{J\,kg^{-1}}$) is the energy per unit mass required for the phase transition. For new ice formation in open water, the new ice thickness must be prescribed (usually 10 cm) and the fractional area is derived from Eq. (7). For surface melting, ΔQ is different from zero only if the surface temperature is at the freezing point.

GMDD
8, 3403–3441, 2015

Snow-ice formation requires negative freeboard, which occurs if the snow load is large enough for the snow–ice interface to lie below sea level (Fichefet and Morales Maqueda, 1997). Seawater is assumed to flood the snow below sea level and freeze there, conserving heat and salt during the process. The associated ocean-to-ice mass flux is:

$$F^{\mathrm{m}} = (\rho_{\mathrm{i}} - \rho_{\mathrm{s}})\frac{\partial h}{\partial t}$$

Every ice–ocean mass exchange involves corresponding energy and salt exchanges (Schmidt et al., 2004). For instance, seawater freezing involves a change in energy $\Delta E = E_{\mathrm{i}}(S,T) - E_{\mathrm{w}}(T_{\mathrm{w}})$, where E_{i} is the internal energy of the frozen ice at its new temperature and salinity and E_{w} is the internal energy of the source seawater at its original temperature. To ensure heat conservation in the ice–ocean system, the heat flux $Q^{\mathrm{m}} = E_{\mathrm{w}}(T_{\mathrm{w}})F^{\mathrm{m}}$ is extracted from the ocean. Conversely, when ice melts the internal energy of melt water is sent to the ocean. Salt exchanges are detailed hereafter.

2.3.3 Salt

The salinity of the new ice formed in open water is determined from ice thickness, using the empirical thickness–salinity relationship of Kovacs (1996). The vertically averaged ice salinity $\overline{S}$ (in ‰) evolves in time following Vancoppenolle et al. (2009a, b) as:

$$\frac{\partial \overline{S}}{\partial t} = \sum_j \left(\frac{v_j S_w - \overline{S}}{h}\right)\frac{\partial h_j}{\partial t} + \sum_j I_j \left(\frac{S_j - \overline{S}}{T_j}\right) \quad (8)$$

The first term on the right-hand side is the salt uptake summed over the three ice growth processes (ii, iii and iv), each characterized by a growth rate $\partial h_j/\partial t$ and a coefficient v_j that determines the fraction of trapped oceanic salinity S_w. For basal freezing, v_j is a function of growth rate (Cox and Weeks, 1988). For snow–ice formation, it is a function of snow and ice densities. For ridging, it depends on ridge porosity. The second

GMDD
8, 3403–3441, 2015

term on the right-hand side is the salt loss summed over the two parameterized brine drainage processes (gravity drainage and flushing; see Notz and Worster, 2009). I_j is 1 if the drainage process is active and 0 if it is not. Gravity drainage occurs if ice is growing at the base; flushing occurs if the snow/ice is melting at the surface. S_j (5 ‰ for gravity drainage; 2 ‰ for flushing) is the restoring salinity for each drainage process and T_j is the corresponding time scale (20 days for gravity drainage, 10 days for flushing).

The shape of the vertical salinity profile depends on $\overline{S}$, so that ice with $\overline{S} > 4.5$ ‰ has a vertically constant profile. By contrast, ice fresher than this threshold has a linear profile with a lower salinity near the surface. This difference is important to properly represent the impact of brine on thermal properties (Vancoppenolle et al., 2005). Ice formation retrieves salt from the ocean but the conjunction with water mass loss makes the ocean surface saltier. Conversely, ice melting releases salt but makes the ocean fresher. Brine drainage is not associated with an exchange of water mass, so the salt release directly increases ocean salinity.

2.3.4 Transport in thickness space

Ice growth or melt in a given category involves a transfer of ice to neighbor categories, which is formally analogous to a transport in thickness space with a velocity equal to the net growth rate $\mathrm{d}h/\mathrm{d}t$. This transport in thickness space is solved using the semi-lagrangian linear remapping scheme of Lispcomb (2001). This scheme is weakly diffusive, converges with a few categories and its computational cost is minimal, an important property since transport operates over each ice category. Transport in thickness space is applied to all other state variables, as well.

GMDD
8, 3403–3441, 2015

3 Control of the mass, salt and heat budgets

3.1 Change in the time stepping scheme

Mass, heat and salt should be perfectly conserved over sufficiently long time scales in an ice–ocean modelling system, especially for climate studies. Moreover, for analysis purpose, the contributions from the different processes should be identified. This has motivated a change in the time stepping scheme as well as in the algorithm used to solve the heat diffusion equation.

The dynamical and thermodynamical time evolutions of the state variables were previously calculated in parallel, starting from the same initial state (Fig. 1a). Both tendencies were then combined to calculate the new state variables. This method, numerically stable and matching NEMO's philosophy required however a final correction step to impose that ice losses (by melting and/or divergence) did not exceed the ice initially available. This correction step could be as important as the physical processes in some cases, and could not be attributed to a specific process.

The modified temporal scheme is sequential (as for LIM2 and CICE), removing the need for a correction step. The ice state variables are first modified by dynamical processes, then by halo-thermodynamics (Fig. 1b). The scheme allows consistent diagnostics of the processes contributing to the atmosphere–ice–ocean exchanges without altering the general model behavior (not shown). This is illustrated in the next section in a global ice–ocean simulation at 2° resolution ORCA2-LIM3.

3.2 Change in the heat diffusion algorithm

The conservation of mass, salt and heat was then carefully inspected, leading to several small corrections. In particular, the scheme used to solve the heat diffusion equation (Eq. 6), a space-centered implicit backward-Euler one (Bitz and Lipscomb, 1999), does not strictly conserve heat. The scheme is the same as in CICE, for which the problem was already reported but was not resolved to our knowledge (Hunke et al., 2013).

GMDD
8, 3403–3441, 2015

Because Eq. (6) is non-linear (E and κ depend on S and T) and both surface and internal layer temperatures evolve at the same time, the numerical procedure has to be iterative until temperature change is less than 10^{-5} °C or after 50 iterations. The scheme does not strictly converge and leads to small errors ~~on~~ in heat flux of $\sim 0.005\,\mathrm{W\,m^{-2}}$, averaged over the ice pack for a global 2° resolution simulation, with maxima reaching in some rare cases $\mathrm{O}(10\,\mathrm{W\,m^{-2}})$. These errors are similar to those reported in CICE user guide ($0.01\,\mathrm{W\,m^{-2}}$, Hunke et al., 2013). Therefore, to ensure strict conservation, either heat fluxes or ice temperature must be further adjusted at the end of iteration. We chose to recalculate the turbulent ocean-to-ice heat flux, subject to large uncertainty and directly involved in the basal energy budget.

3.3 Other changes

3.3.1 Category boundaries

The original discretization of the thickness category boundaries follows the hyperbolic tangent formulation from CICE (Hunke et al., 2013). The formulation proved to be suitable to simulate the Arctic ice pack with only five ice categories, but is hardly adaptable to different ice conditions. For instance, thin ice can only be finely discretized by augmenting the number of ice categories, and de facto increasing computational cost. Multiple simulations, in particular for regional configurations, call for more flexibility without additional cpu consumption. Therefore, a new discretization was implemented that can adjust the expected mean ice thickness $\overline{h}$ over the domain. Category boundaries lie between 0 and $3\overline{h}$ and are determined using a fitting function proportional to $(1+h)^{-\alpha}$, where $\alpha = 0.05$. For $\overline{h} = 2$ m, the new formulation is very similar to the original one. For $\overline{h} = 1$ m, boundaries tighten within 3 m, providing more resolution for thin ice (Fig. 2).

GMDD
8, 3403–3441, 2015

3.3.2 In and outputs

LIM3 has been completely interfaced with XIOS (XML Input Output Server: http://forge.ipsl.jussieu.fr/ioserver/), a new and innovative library developed at Institut Pierre-et-Simon Laplace (IPSL) and dedicated to climate modelling data output. XIOS combines flexibility and performance. It considerably simplifies output definition and management by outsourcing output description in an external XML file. In addition, the interface offers numerous possibilities of variables manipulation such as complex temporal operations and computations involving several variables. XIOS also achieves excellent performance to output data on massively parallel supercomputers by using several "server" processes exclusively dedicated to data writing. File system writing is totally overlapped by computation.

3.4 Global ice–ocean simulation: ORCA2-LIM3

3.4.1 Experimental setup and observation datasets

The simulation presented here uses the most recent 3.6 version of NEMO. It comprises the ocean general circulation model OPA version 3.6 (Madec, 2008) and LIM (Vancoppenolle et al., 2009b) in its 3.5 version presented above, running on the same tripolar 2° resolution grid (ORCA2). More details can be found in Mignot et al. (2013). The atmospheric state is imposed using the CORE normal year forcing set proposed by Large and Yeager (2009). This forcing was developed to inter-compare ice–ocean models (e.g. Griffies et al., 2009). It is based on a combination of NCEP/NCAR reanalyzes (for wind, temperature and humidity) and various satellite products (for radiation), has a 2° resolution and near zero global mean heat and freshwater fluxes. The so-called normal year dataset superimposes the 1995 synoptic variability on the mean 1984–2000 seasonal cycle. The simulation lasts 100 years, much longer than needed for sea ice to reach equilibrium. Most diagnostics presented hereafter are seasonal averages over the last 10 years of the simulation. The computational cost of such a simulation is about

GMDD
8, 3403–3441, 2015

24 h on 32 processors of an IBM-x3750, with LIM3.5 consuming less than 20 % of this time.

The observed ice extent is derived from ice concentration retrievals of the EUMETSAT Ocean and Sea Ice Satellite Application Facility (OSI-SAF, Eastwood et al., 2010) and is presented here as 1984–2000 monthly means. For ice volume, since there are no direct observations, we use instead the 1979–2011 reanalysis PIOMAS in the Arctic (Schweiger et al., 2011), and the NEMO-LIM2-EnKF reconstruction in the Antarctic (Massonnet et al., 2013).

3.4.2 Ice concentration and thickness

The new capabilities of LIM3.5 are illustrated in this section. Neither the model nor the atmospheric forcing are tuned to get the most realistic sea ice simulation, since it is not the purpose of this study. Instead, we choose the model default parameters and show that the simulated ice concentrations and thicknesses are in reasonable agreement with observations.

Figure 3 shows the ice concentrations at the model maximum and minimum extent in ORCA2-LIM3 and OSI-SAF (March and September for the Arctic; February and September for the Antarctic). The simulated ice distribution is relatively close to the observations, even though in boreal winter ice extends too much southward, covering a large part of the Greenland Sea while it almost disappears near Antarctica. In the Northern Hemisphere, the extent bias is a typical drawback of low resolution simulation. It is attributed to ~~low an~~ a low? ocean heat supply by the North Atlantic Current and to an overestimated ice volume export through Fram Strait (by about 20 %). In the Southern Hemisphere, the ice loss is linked to the low resolution of the wind forcing and to an overestimated ocean convective activity, which melts ice by mixing relatively warm and salty water at depth with cold and fresh surface waters.

The seasonal cycle of the sea ice extent (i.e. the area enclosed within the 15 % ice concentration contour, white lines in Fig. 3) is presented in Fig. 4 for both hemispheres. In the Northern Hemisphere, the observed ice extent varies seasonally between 8 and

GMDD
8, 3403–3441, 2015

16×10^6 km^2. The simulation gives very similar variations. In the Southern Hemisphere, the observed ice extent varies from a minimum of 4×10^6 km^2 in February to a maximum of 20×10^6 km^2 in September. The model reproduces the amplitude of the observed seasonal variations but ~~is biased low by~~ has a low bias of 3×10^6 km^2 all year long due to the wrong position of the Antarctic Circumpolar Current and too strong ~~a~~ vertical ocean mixing, which is a classic problem in global ocean models (Kim and Stössel, 2001).

The simulated ice thickness distributions in March and September are displayed in Fig. 5 for both hemispheres. The ice thickness exceeds 3 m in the Central Arctic, reaching 4.5 m along the Canadian and Greenland coasts. This is in good agreement with the submarine thickness retrievals (3.4 m in the Central Arctic in February–March 1988; Kwok and Rothrock, 2009). IceSat thickness retrievals for February–March 2004–2008 are lower (2.2 m, not shown), which is consistent with the recent Arctic sea ice thinning. The simulated Arctic ice volume varies from a minimum of 13 000 km^3 in September to a maximum of 30 000 km^3 in March–April. This is very similar to PIOMAS reanalyzes. In the Southern Hemisphere, the maximum ice thickness is about 2 m in the Weddell Sea and next to Ross Sea. Simulated ice volume variations (0 to 12 000 km^3) is likely biased low, but in broad agreement with reanalysis (2 000–10 000 km^3, F. Massonnet, personal communication, 2015) and satellite estimates (Kurtz and Markus, 2012).

Overall the simulation is in reasonable agreement with available observations of ice thickness and concentration even though no tuning has been done, and we can now focus on the ice budgets.

3.4.3 Mass and salt balances

The new developments allow to split the ice mass, heat and salt budgets seasonally and over the different processes. Seven processes affect the ice mass (see Sect. 2.3.2). Five belong to vertical thermodynamics: new ice growth in open water, basal growth and melt, surface melt, and snow–ice formation. Two are dynamical processes: advection and entrapment and freezing of seawater in newly built ridges. Changes in the heat

GMDD
8, 3403–3441, 2015

and salt contents involve the same processes, plus the changes in internal temperatures (for heat budget) and internal salinity due to brine drainage (for salt budget).

We focus on the mass budget for illustration and present the different contributions integrated over the Northern and Southern Hemispheres in Fig. 6. In both hemispheres, the dominant balance is between basal ice growth and melt. Surface melting is also important but only in the Arctic during boreal summer. Contributions of secondary importance are new ice formation in open water during the cold season (both hemispheres) and snow–ice formation during Antarctic spring. Note that the contribution from advection is obviously nil when integrated over a hemisphere. The maximum growth rate is about the same in both hemispheres (slightly up to 20 cm month^{-1}). Basal melt is remarkably weaker in the Arctic than in the Antarctic (maximum at 40 and 65 cm month^{-1}, respectively). This is because in the Arctic, the ice is constrained by continents to stay at high latitudes, where the ocean stratification is strong and the ocean heat flux is weak. Overall, about 26 000 km^3 of ice are formed and melted each year in the Arctic, which corresponds to about 2 m of ice. About 330 Gt of salt are extracted from the ocean during freezing and released during ice desalinization and melting. These mean values are similar in the Antarctic though slightly lower: 21 000 km^3 of ice of annual ice production ($\sim$ 1.8 m) and 290 Gt of salt.

This integrated view masks strong geographic disparities. In Fig. 7 we show the geographical distribution of some of the processes in March in the Arctic. The interior of the ice pack still grows from the bottom, while the base of the ice edge melts, resulting in snow–ice formation where snow is thick enough. As expected, the strongest thickness changes due to advection are near the ice edge. Ice formation in open water is globally weak but becomes one of the main processes in some regions of climate importance (see next section).

GMDD
8, 3403–3441, 2015

4 Regional configurations

4.1 Boundary conditions for a multi-category sea ice model

NEMO can also be used in regional configurations. Appropriate boundary conditions must be prescribed, with possible inflows/outflows through open boundaries. The BDY tool was specifically designed to handle this in NEMO (Chanut, 2005). Ocean temperature, salinity and baroclinic velocity are treated with a flow relaxation scheme (Engedahl, 1995), while the Flather (1976) radiation condition is well suited for tidal forcing and therefore is used for both the barotropic ocean velocity and sea surface height. Sea ice was not taking into account in the reference version of BDY, which restricted the use of regional configurations to ice-free areas. New developments to BDY were introduced to accommodate sea ice. The approach is simple and gives satisfying results.

The sea ice state variables depend on the direction of ice velocity in a way similar to an upstream advection scheme. They are relaxed toward interior domain values where ice exits the domain, and toward external boundary data where ice enters the domain. External boundary data can either come from observations, reanalyzes or reference simulations. As ice velocities in these external files are not always well determined, they need to be defined at the boundary. Tangent ice velocity is always set to 0. Normal ice velocity depends on the presence of ice in the adjacent cell: if ice-free, ice velocity is assumed to be relaxed to ocean velocity; otherwise ice velocity is relaxed to the velocity of the adjacent cell.

Most boundary datasets do not include multiple ice categories. Hence, a strategy to fill in thickness categories in a smooth and consistent way with the external data set was defined. The category-filling algorithm used to initialize the sea ice state variables in the L categories from prescribed thickness $\overline{h}$ and concentration A was used (Vancoppenolle et al., 2012). The category where $\overline{h}$ lies has the largest ice concentration $A/\sqrt{L}$. The other categories are filled assuming a Gaussian distribution, in a volume-conserving way, preserving positivity.

GMDD
8, 3403–3441, 2015

4.2 Simulation around the Svalbard Archipelago

4.2.1 Experimental setup

To illustrate the capability of NEMO-LIM3 in regional ice-covered domains, we designed an experiment in a regional configuration (500 km × 500 km) around the Svalbard Archipelago. This region was chosen because of the strong tides and the diverse conditions encountered. A tidal gauge at Ny-Alesund, on the west coast of Svalbard, recorded tidal amplitudes up to 2 m. North of the archipelago, lies the perennial ice pack of the Arctic Ocean transitioning southwards to a seasonal ice zone. The domain also includes the large Storfjorden polynya, frequently open during winter. Polynyas are small (10–10^5 km^2) and sporadic by nature, but their role for climate is considerable (e.g. Morales Maqueda et al., 2004). In winter, the ocean heat loss in polynyas is considerable, producing large amounts of sea ice, as well as dense water sinking towards the deep ocean basins. At the onset of melting season, polynyas enhance ice melting as the open waters captures more heat than ice-covered areas.

Horizontal resolution is very high (2–3 km) in order to properly represent fine-scale processes taking place in polynyas. The basin is vertically discretized by 75 non-uniform levels, with a resolution of 1 m at the surface. The domain is open at the four boundaries and conditions there are set up using the BDY tool, modified as described above. Bathymetry is interpolated from etopo1 (Amante and Eakins, 2009), which actually retrieves data from IBCAOv2 north of 64° N (Jakobsson et al., 2008). Tides are important drivers for high frequency processes. Therefore they are included here as well as the non-linear free surface (z^* coordinates system). A third-order upstream biased advection scheme is used for ocean tracers and momentum instead of the flux corrected transport used in ORCA2-LIM3. k-ε closure scheme using generic length scale turbulent mixing is chosen (Umlauf and Burchard, 2003; Reffray et al., 2015). The simulation is forced at the surface by 6 hourly, 3/4° × 3/4° ERAI dataset, and at the boundaries by 5 days outputs from a DRAKKAR 1/4° global reference simulation ORCA025-MJM (an update to ORCA025-G70; Barnier et al., 2006; Molines et al.,

GMDD
8, 3403–3441, 2015

2007; Drakkar group, 2007). We also prescribe tidal sea surface height and barotropic velocity at the boundaries from FES2012 (Carrère et al., 2012). The simulation is conducted over 1999–2009 in order to capture interannual variability.

The model behavior at the boundary is satisfactory. No noise or wave reflection pollutes the basin despite strong in and out flows and the presence of tides (not shown). The simulation is also able to represent transient polynya occurrence. As an example, Fig. 8 shows the simulated ice concentrations on 22 May 2002 around Svalbard (right panel), as well as the corresponding observations (left panel). At this date, northeastern winds were sufficiently strong to open the Storfjorden polynya by pushing sea ice towards the western side of the fjord. The opening of polynyas is generally reasonably well represented by the simulation, in Storfjorden and elsewhere, though it is somewhat smaller than observed. This is likely due to the low spatio-temporal variability of the ERAI surface forcing, as highlighted by previous studies (Skogseth et al., 2007). Downscaling the forcing with a regional atmospheric model is probably required to further improve the simulation.

4.2.2 Mass and salt balances in Storfjorden

Figure 9 shows the 10 year variability of the different mass balance processes over the 13 000 km^2 of the Storfjorden region (see Fig. 8). The sea ice mass balance is dominated by basal growth (16 $km^3\,year^{-1}$) and new ice growth in open water (12 $km^3\,year^{-1}$), compensated by export out of the domain (not shown) and basal melt (11 $km^3\,year^{-1}$). Surface melt can be significant (up to one third of total melt) but only at the beginning of summer. As expected, ice growth in open water is a crucial process here, while it is generally weak globally in the Arctic (see previous section). The net ice production is +17 $km^3\,year^{-1}$ on average, with strong inter-annual variability (from 23 km^3 in 2001–2002 to 10 km^3 in 2006–2007). This corresponds to a salt flux from the ocean to the ice of about 150 $Mt\,year^{-1}$. Over a year, the net production almost balances ice export (not shown), so there is no long-term accumulation of ice in the basin. However, at time scales shorter than a year, ice can pile up in the Storfjorden.

GMDD
8, 3403–3441, 2015

By combining AMSR-E sea ice concentrations and an atmospheric forcing from ERA-interim, Jardon et al. (2014) estimated a mean ice production of 47 km^3 in winter between 2002 and 2011. With a similar approach, Skogseth et al. (2004) found a mean ice production of 40 km^3 during 1998–2002. In our simulation, this production amounts to 33 km^3 for the period 1999–2009. This value is reasonable, though it is smaller than observational retrievals and reanalyzes. This could be due to the relative coarseness of the ERAI surface forcing fluxes or to the interactive ocean processes.

5 Conclusions

The Louvain-la-Neuve sea ice model (LIM) has considerably evolved during the past decade. Two versions were developed and coexist up to now. LIM2 is based on a Hibler (1979) mono-category approach, and was integrated in the NEMO system about one decade ago (Timmermann et al., 2005). LIM2 was the reference model so far and was used in a variety of simulations including CMIP5. LIM3 is a more sophisticated model developed 5 years ago (Vancoppenolle et al., 2009a), including a better representation of sub-grid scale ice thickness distribution and salinity processes. Several modifications to LIM3 were made to make it more robust and versatile, leading to LIM3.5, described in this paper. LIM3.5 is the reference model for the forthcoming CMIP6 simulations.

Robustness and versatility of LIM3 have been improved, so that the ice code can be used at various resolutions and domain sizes. Three main developments were required. First, the general time stepping of the code is changed from parallel to sequential. In other words, thermodynamics processes are now performed after dynamics, which enables to discriminate the different processes responsible for the mass, heat and salt exchanges across the interfaces between air, ice and ocean. Second, conservation in the code was carefully examined by comparing these exchanges with thermodynamical and dynamical ice evolution, which has led to several small corrections to reach a strictly conservative code. In particular, the iterative procedure to solve the heat diffusion equation (Eq. 6) did not exactly converge, leading to small heat leaks. The leaks

GMDD
8, 3403–3441, 2015

are now corrected by recalculating heat fluxes. Finally, version 3.5 of LIM is the first to handle open boundary conditions for regional simulations in ice-covered areas. The sea ice state variables at the boundary depends on the direction of the normal ice velocity to allow realistic in and outflows with the rest of the ocean. Boundary conditions are flexible enough so that ice boundary datasets can either integrate a sub-grid scale ice thickness distribution or not.

To illustrate the new capabilities of LIM3, we showed 100 years of the 2° resolution forced simulation ORCA2-LIM3, and 10 years of a regional simulation at 2 km resolution around the Svalbard Archipelago, which hosts the recurrent Storfjorden polynya. We mainly focused on the ice mass budget and show how they differ, depending on the region studied. At the global scale, the dominant processes are basal ice growth and basal ice melt for both hemispheres, but other processes matter locally. In the Storfjorden, new ice growth in open water is nearly as large as basal growth. The entire ice production is exported out of Storfjorden annually, with large interannual variability over the 10 years of the experiment (1999–2009), with maximum values exceeding twice the minimum.

Version 3.5 of LIM3 is incorporated in the reference version of NEMO (currently v3.6) and can be downloaded from the NEMO web site (http://www.nemo-ocean.eu/) at this address:

https://forge.ipsl.jussieu.fr/nemo/browser/trunk/NEMOGCM/NEMO/LIM_SRC_3.

LIM2 is no longer the reference and will be discontinued in the next NEMO release.

There are also ongoing and upcoming developments for LIM.

1. As some applications could still need a mono-category ice model (either for physical or computational reasons), LIM3.5 also includes mono-category parameterizations that will be described in a publication in preparation.

2. The compatibility between the Adaptive Grid Refinement In Fortran (AGRIF; Debreu et al., 2008) and LIM3 to run global simulations is yet to achieve and work is

GMDD
8, 3403–3441, 2015

in progress to use the LIM2-AGRIF interface (Talandier et al., 2014) and apply it to LIM3.

3. The melt pond parameterization of Flocco and Feltham (2007), as implemented by Lecomte et al. (2015), exists in a branch of the code and is expected soon in the reference version.

In the future, LIM will continue to be developed, including, among others, sea ice biogeochemistry (Vancoppenolle and Tedesco, 2015; Moreau et al., 2015), an elasto-brittle rheology (Girard et al., 2011), improved snow physics (Lecomte et al., 2013, 2015), and a subgrid-scale representation of ice–ocean exchanges (Barthélemy et al., 2015).

Acknowledgements. The present work was supported by the French National Research Agency (ANR) as part of the OPTIMISM project (ANR-09-BLAN-0227-01), the European Community's Seventh Framework Program FP7/SPACE (MyOcean2, grant 283367), IS-ENES2 (grant 312979) and BICICLO (FP7 CIG 321938). Computational resources have been provided by the French Institut du Développement et des Ressources en Informatique Scientifique (IDRIS). The Antarctic sea ice concentration reprocessed dataset was provided by the Ocean and Sea Ice Satellite Application Facilities (OSISAF) and is available at http://osisaf.met.no. The MODIS image is courtesy of the online Data Pool at the NASA Land Processes Distributed Active Archive Center (LP DAAC), USGS/Earth Resources Observation and Science (EROS) Center, Sioux Falls, South Dakota (https://lpdaac.usgs.gov/data_access).

References

Aagaard, K. A. and Carmack, E. C.: The role of sea ice and other fresh water in the Arctic circulation, J. Geophys. Res., 94, 14485–14498, 1989.

Amante, C. and Eakins B. W.: ETOPO1 1 arc-minute global relief model: procedures, data sources and analysis, US Department of Commerce, National Oceanic and Atmospheric Administration, National Environmental Satellite, Data, and Information Service, National Geophysical Data Center, Marine Geology and Geophysics Division, 2009.

GMDD

8, 3403–3441, 2015

Atkinson, A., Siegel, V., Pakhomov, E., and Rothery, P.: Long-term decline in krill stock and increase in salps within the Southern Ocean, Nature, 432, 100–103, 2004.
Barnier, B., Madec, G., Penduff, T., Molines, J.-M., Treguier, A.-M., Le Sommer, J., Beckmann, A., Biastoch, A., Böning, C., Dengg, J., Derval, C., Durand, E., Gulev, S., Remy, E., Talandier, C., Theetten, S., Maltrud, M., McClean, J., and De Cuevas, B.: Impact of partial steps and momentum advection schemes in a global ocean circulation model at eddy-permitting resolution, Ocean Dynam., 56, 543–567, doi:10.1007/s10236-006-0082-1, 2006.
Barthélemy, A., Fichefet, T., Goosse, H., and Madec, G.: Modelling the interplay between sea ice formation and the oceanic mixed layer: limitations of simple brine rejection parameterizations, Ocean Model., 86, 141–152, 2015.
Bitz, C. M. and Lipscomb, W. H.: An energy-conserving thermodynamic model of sea ice, J. Geophys. Res., 104, 15669–15677, 1999.
Bitz, C. M., Holland, M. M., Weaver, A. J., and Eby, M.: Simulating the ice-thickness distribution in a coupled climate model, J. Geophys. Res., 106, 2441–2463, 2001.
Bouillon, S., Morales Maqueda, M. A., Fichefet, T., and Legat, V.: An elastic–viscous–plastic sea ice model formulated on Arakawa B and C grids, Ocean Model., 27, 174–184, 2009.
Bouillon, S., Fichefet, T., Legat, V., and Madec, G.: The elastic–viscous–plastic method revisited, Ocean Model., 71, 2–12, 2013.
Budyko, M. I.: The effect of solar radiation variations on the climate of the Earth, Tellus, 5, 611–619, 1969.
Carrère, L., Lyard, F., Cancet, M., Guillot, A., and Roblou, L.: FES2012: A new global tidal model taking advantage of nearly 20 years of altimetry, in: Proceedings of meeting, vol. 20, 2012.
Chanut, J.: Nesting code for NEMO, European Union: Marine Environment and Security for the European Area (MERSEA) Integrated Project, ref: MERSEA-WP09-MERCA-TASK-9.1.1, 24 pp., Mercator Ocean, 2005.
Comiso, J. C.: Variability and trends of the global sea ice cover, in: Sea ice, 2nd edn., edited by: Thomas D. N. and Dieckmann, G. S., Wiley, 2, 205–246, 2010.
Connolley, W. M., Gregory, J. M., Hunke, E. C., and McLaren, A. J.: On the consistent scaling of terms in the sea-ice dynamics equation, J. Phys. Oceanogr., 34, 1776–1780, 2004.
Cox, G. F. N. and Weeks, W. F.: Numerical simulations of the profile properties of undeformed first-year sea ice during growth season, J. Geophys. Res., 93, 1244–12460, 1988.

GMDD
8, 3403–3441, 2015

Croxall, J. P., Trathan, P. N., and Murphy, E. J.: Environmental change and Antarctic seabird populations, Science, 297, 1510–1514, 2002.

Danabasoglu, G., Yeager, S. G., Bailey, D., Behrens, E., Bentsen, M., Bi, D., Biastoch, A., Boening, C., Bozec, A., Canuto, V. M., Cassou, C., Chassignet, E., Coward, A. C., Danilov, S., Diansky, N., Drange, H., Farneti, R., Fernandez, E., Fogli, P. G., Forget, G., Fujii, Y., Griffies, S. M., Gusev, A., Heimbach, P., Howard, A., Jung, T., Kelley, M., Large, W. G., Leboissetier, A., Lu, J., Madec, G., Marsland, S. J., Masina, S., Navarra, A., Nurser, A. J. G., Pirani, A., Salasy Melia, D., Samuels, B. L., Scheinert, M., Sidorenko, D., Treguier, A.-M., Tsujino, H., Uotila, P., Valcke, S., Voldoire, A., and Wang, Q.: North Atlantic simulated in Coordinated Ocean-ice Reference Experiments phase II CORE-II), Part I: Mean states, Ocean Model., 73, 76–107, 2014.

Debreu, L., Vouland, C., and Blayo, E.: AGRIF: adaptive grid refinement in Fortran, Comput. Geosci., 34, 8–13, 2008.

DRAKKAR Group: Eddy-permitting ocean circulation windcasts of past decades, CLIVAR Exchanges, No. 12, International CLIVAR Project Office, Southampton, United Kingdom, 8–10, 2007.

Dufresne, J.-L., Foujols, M.-A., Denvil, S., Caubel, A., Marti, O., Aumont, O., Balkanski, Y., Bekki, S., Bellenger, H., Benshila, R., Bony, S., Bopp, L., Braconnot, P., Brockmann, P., Cadule, P., Cheruy, F., Codron, F., Cozic, A., Cugnet, D., de Noblet, N., Duvel, J.-P., Ethé, C., Fairhead, L., Fichefet, T., Flavoni, S., Friedlingstein, P., Grandpeix, J.-Y., Guez, L., Guilyardi, E., Hauglustaine, D., Hourdin, F., Idelkadi, A., Ghattas, J., Joussaume, S., Kageyama, M., Krinner, G., Labetoulle, S., Lahellec, A., Lefebvre, M.-P., Lefevre, F., Levy, C., Li, Z.-X., Lloyd, J., Lott, F., Madec, G., Mancip, M., Marchand, M., Masson, S., Meurdesoif, Y., Mignot, J., Musat, I., Parouty, S., Polcher, J., Rio, C., Schulz, M., Swingedouw, D., Szopa, S., Talandier, C., Terray, P., and Viovy, N.: Climate change projections using the IPSL-CM5 Earth System Model: from CMIP3 to CMIP5, Clim. Dynam., 40, 2123–2165, 2013.

Eastwood, S., Larsen, K. R., Lavergne, T., Nielsen, E., and Tonboe, R.: Global Sea Ice Concentration Reprocessing Product User Manual, Product OSI-409, The EUMETSAT Network of Satellite Appl. Fac., 2010.

Engedahl, H.: Use of the flow relaxation scheme in a three-dimensional baroclinic ocean model with realistic topography, Tellus A, 47, 365–382, 1995.

Fichefet, T. and Morales Maqueda, M. A.: Sensitivity of a global sea ice model to the treatment of ice thermodynamics and dynamics, J. Geophys. Res., 102, 12609–12646, 1997.

GMDD
8, 3403–3441, 2015

Flather, R. A.: A tidal model of the North-west European continental shelf, Mem. Soc. R. Sci. Liège, 6, 141–164, 1976.
Flato, G. M. and Hibler, W. D.: Ridging and strength in modeling the thickness distribution of Arctic sea ice, J. Geophys. Res., 100, 18611–18626, 1995.
Flato, G., Marotzke, J., Abiodun, B., Braconnot, P., Chou, S. C., Collins, W., Cox, P., Driouech, F., Emori, S., Eyring, V., Forest, C., Gleckler, P., Guilyardi, E., Jakob, C., Kattsov, V., Reason, C., and Rummukainen, M.: Evaluation of climate models, In: Climate Change 2013: The Physical Science Basis. Contribution of Working Group I to the Fifth Assessment Report of the Intergovernmental Panel on Climate Change, pp. 741–866, Cambridge University Press, 2013.
Girard, L., Bouillon, S., Weiss, J., Amitrano, D., Fichefet, T., and Legat, V.: A new modeling framework for sea-ice mechanics based on elasto-brittle rheology, Ann. Glaciol., 52, 123–132, 2011.
Goosse, H. and Fichefet, T.: Importance of ice–ocean interactions for the global ocean circulation: a model study, J. Geophys. Res., 104, 23337–23355, 1999.
Griffies, S. M., Biastoch, A., Böning, C., Bryan, F., Danabasoglu, G., Chassignet, E. P., England, M. H., Gerdes, R., Haak, H., Hallberg, R. W., Hazeleger, W., Jungclaus, J., Large, W. G., Madec, G., Pirani, A., Samuels, B. L., Scheinert, M., Gupta, A. S., Severijns, C. A., Simmons, H. L., Treguier, A. M., Winton, M., Yeager, S., and Yin, J.: Coordinated Ocean-ice Reference Experiments (COREs), Ocean Model., 26, 1–46, doi:10.1016/j.ocemod.2008.08.007, 2009.
Haapala, J.: On the modeling of ice thickness redistribution, J. Glaciol., 46, 427–437, 2000.
Hazeleger, W., Severijns, C., Semmler, T., Stefanescu, S., Yang, S., Wang, X., Wyser, K., Dutra, E., Baldasano, J. M., Bintanja, R., Bougeault, P., Caballero, R., Ekman, A. M. L., Christensen, J. H., van den Hurk, B., Jimenez, P., Jones, C., Kållberg, P., Koenigk, T., McGrath, R., Miranda, P., Van Noije, T., Palmer, T., Parodi, J. A., Schmith, T., Selten, F., Storelvmo, T., Sterl, A., Tapamo, H., Vancoppenolle, M., Viterbo, P., and Willén, U.: EC-earth: a seamless earth-system prediction approach in action, B. Am. Meteorol. Soc., 91, 1357–1363, 2010.
Hibler III, W. D.: A dynamic–thermodynamic sea ice model, J. Phys. Oceanogr., 9, 815–846, 1979.
Hibler III, W. D.: Modeling a variable thickness sea ice cover, Mon. Weather Rev., 108, 194–1973, 1980.

GMDD
8, 3403–3441, 2015

Høyland, K. V.: Consolidation of first-year sea ice ridges, J. Geophys. Res., 107, 3062, doi:10.1029/2000JC000526, 2002.
Hunke, E. C. and Dukowicz, J. K.: An elastic-viscous-plastic model for sea ice dynamics, J. Phys. Oceanogr., 27, 1849–1867, 1997.
Hunke, E. C., Lipscomb, W. H., Turner, A. K., Jeffery, N., and Elliott, S.: CICE: the Los Alamos Sea Ice Model Documentation and Software User's Manual Version 5.0 LA-CC-06-012, Los Alamos National Laboratory, Los Alamos NM, 87545, 115, 2013.
Jakobsson, M., Macnab, R., Mayer, M., Anderson, R., Edwards, M., Hatzky, J., Schenke, H.-W., and Johnson, P.: An improved bathymetric portrayal of the Arctic Ocean: implications for ocean modeling and geological, geophysical and oceanographic analyses, Geophys. Res. Lett., 35, L07602, doi:10.1029/2008GL033520, 2008.
Jardon, F. P., Vivier, F., Bouruet-Aubertot, P., Lourenço, A., Cuypers, Y., and Willmes, S.: Ice production in Storfjorden (Svalbard) estimated from a model based on AMSR-E observations: impact on water mass properties, J. Geophys. Res.-Oceans, 119, 377–393, doi:10.1002/2013JC009322, 2014.
Kim, S. J. and Stössel, A.: Impact of subgrid-scale convection on global thermohaline properties and circulation, J. Phys. Oceanogr., 31, 656–674, 2001.
Kurtz, N. T. and Markus, T.: Satellite observations of Antarctic sea ice thickness and volume, J. Geophys. Res., 117, C08025, doi:10.1029/2012JC008141, 2012.
Kwok, R. and Rothrock, D. A.: Decline in Arctic sea ice thickness from submarine and ICESat records: 1958–2008, Geophys. Res. Lett., 36, L15501, doi:10.1029/2009GL039035, 2009.
Large, W. G. and Yeager, S. G.: The global climatology of an interannually varying air–sea flux data set, Clim. Dynam., 33, 341–364, 2009.
Lecomte, O., Fichefet, T., Vancoppenolle, M., Domine, F., Massonnet, F., Mathiot, P., Morin, S., and Barriat, P. Y.: On the formulation of snow thermal conductivity in large-scale sea ice models, J. Adv. Model. Earth Syst., 5, 542–557, doi:10.1002/jame.20039, 2013.
Lecomte, O., Fichefet, T., Flocco, D., Schroeder, D., and Vancoppenolle, M.: Interactions between wind-blown snow redistribution and melt ponds in a coupled ocean-sea ice model, Ocean Model., 87, 67–80, 2015.
Leppäranta, M., Lensu, M., Koslof, P., and Witch, B.: The life story of a first-year sea ice ridge, Cold Reg. Sci. Technol., 23, 279–290, 1995.
Lipscomb, W. H.: Remapping the thickness distribution in sea ice models, J. Geophys. Res., 106, 13989–14000, 2001.

GMDD
8, 3403–3441, 2015

Lipscomb, W. H., Hunke, E. C., Maslowski, W., and Jakacki, J.: Improving ridging schemes for high-resolution sea ice models, J. Geophys. Res., 112, C03S91, doi:10.1029/2005JC003355, 2007.
Madec, G.: NEMO Ocean Engine, Note du Pole de modélisation, Institut Pierre-Simon Laplace (IPSL), Paris, France, no. 27, ISSN No 1288–1619, 2008.
Massonnet, F., Mathiot, P., Fichefet, T., Goosse, H., Beatty, C. K., Vancoppenolle, M., and Lavergne, T.: A model reconstruction of the Antarctic sea ice thickness and volume changes over 1980–2008 using data assimilation, Ocean Model., 64, 67–75, 2013.
Mignot, J., Swingedouw, D., Deshayes, J., Marti, O., Talandier, C., Séférian, R., and Madec, G.: On the evolution of the oceanic component of the IPSL climate models from CMIP3 to CMIP5: a mean state comparison, Ocean Model., 72, 167–184, 2013.
Molines, J.-M., Barnier, B., Penduff, T., Brodeau, L., Treguier, A.-M., Theetten, S., and Madec, G.: Definition of the interannual experiment ORCA025-G70, 1958–2004, LEGI report LEGI-DRA-2-11-2006, available at: www.ifremer.fr/lpo/drakkar (last access: September 2007), 2006.
Morales Maqueda, M. A., Willmott, A. W., and Biggs, N. R. T.: Polynya dynamics: a review of observations and modelling, Rev. Geophys., 42, RG1004, doi:10.1029/2002RG000116, 2004.
Moreau, S., Vancoppenolle, M., Delille, B., Tison, J.-L., Zhou, J., Kotovitch, M., Thomas, D. N., Geilfus, N.-X., and Goosse, H.: Drivers of inorganic carbon dynamics in first-year sea ice: a model study, J. Geophys. Res.-Oceans, 120, 471–495, doi:10.1002/2014JC010388, 2015.
Notz, D. and Worster, M. G.: Desalination processes in sea ice, J. Geophys. Res., 114, C05006, doi:10.1029/2008JC004885, 2009.
Prather, M.: Numerical advection by conservation of second-order moments, J. Geophys. Res., 91, 6671–6681, 1986.
Pringle, D. J., Eicken, H., Trodahl, H. J., and Backstrom, L. G. E.: Thermal conductivity of landfast Antarctic and Arctic sea ice, J. Geophys. Res., 112, C04017, doi:10.1029/2006JC003641, 2007.
Reffray, G., Bourdalle-Badie, R., and Calone, C.: Modelling turbulent vertical mixing sensitivity using a 1-D version of NEMO, Geosci. Model Dev., 8, 69–86, doi:10.5194/gmd-8-69-2015, 2015.
Rothrock, D. A.: The energetics of the plastic deformation of pack ice by ridging, J. Geophys. Res., 80, 4514–4519, 1975.

GMDD
8, 3403–3441, 2015

Schmidt, G. A., Bitz, C. M., Mikolajewicz, U., and Tremblay, L.-B.: Ice–ocean boundary conditions for coupled models, Ocean Model., 7, 59–74, 2004.
Schweiger, A., R. Lindsay, J. Zhang, M. Steele, and Stern, H.: Uncertainty in modeled arctic sea ice volume, J. Geophys. Res., 116, C000D06, doi:10.1029/2011JC007084, 2011.
Scoccimarro, E., Gualdi, S., Bellucci, A., Sanna, A., Fogli, P. G., Manzini, E., Vichi, M., Oddo, P., and Navarra, A.: Effects of tropical cyclones on ocean heat transport in a high resolution coupled general circulation model, J. Climate, 24, 4368–4384, 2011.
Semtner Jr., A. J.: A model for the thermodynamic growth of sea ice in numerical investigations of climate, J. Phys. Oceanogr., 6, 379–389, 1976.
Shine, K. P. and Henderson-Sellers, A.: The sensitivity of a thermodynamic sea ice model to changes in surface albedo parameterization, J. Geophys. Res., 90, 2243–2250, 1985.
Skogseth, R., Haugan, P. M., and Haarpaintner, J.: Ice and brine production in Storfjorden from four winters of satellite and in situ observations and modeling, J. Geophys. Res., 109, C10008, doi:10.1029/2004JC002384, 2004.
Skogseth, R., Sandvik, A. D., and Asplin, L.: Wind and tidal forcing on the meso-scale circulation in Storfjorden, Svalbard, Cont. Shelf Res., 27, 208–227, 2007.
Talandier, C., Deshayes, J., Tréguier, A.-M., Capet, X., Benshila, R., Debreu, L., Dussin, R., Molines, J.-M., and Madec, G.: Improvements of simulated western North Atlantic current system and impacts on AMOC, Ocean Model., 76, 1–19, doi:10.1016/j.ocemod.2013.12.007, 2014.
Timmermann, R., Goosse, H., Madec, G., Fichefet, T., Ethé, C., and Dulière, V.: On the representation of high-latitude processes in the ORCA-LIM global coupled se ice–ocean model, Ocean Model., 8, 175–201, 2005.
Thomas, D. N. and Dieckmann, G. S.: Sea Ice, 2nd edn., Wiley-Blackwell, Oxford, UK, 2010.
Thorndike, A. S.: Diffusion of sea ice, J. Geophys. Res., 91, 7691–7696, 1986.
Thorndike, A. S., Rothrock, D. A., Maykut, G. A., and Colony, R.: The thickness distribution of sea ice, J. Geophys. Res., 80, 4501–4513, 1975.
Tuhkuri, J. and Lensu, M.: Laboratory tests on ridging and rafting of ice sheets, J. Geophys. Res., 107, 3125, doi:10.1029/2001JC000848, 2002.
Umlauf, L. and Burchard, H.: A generic length-scale equation for geophysical turbulence models, J. Mar. Res., 61, 235–265, doi:10.1357/002224003322005087, 2003.
Untersteiner, N.: Calculations of temperature regime and heat budget of sea ice in the Central Arctic, J. Geophys. Res., 69, 4755–4766, 1964.

GMDD
8, 3403–3441, 2015

Vancoppenolle, M. and Tedesco, L.: Numerical models of sea ice biogeochemistry, in: Sea Ice, 3rd edn., edited by: Thomas, D. N., Wiley-Blackwell, Oxford, UK, 2015.
Vancoppenolle, M., Fichefet, T., and Bitz, C. M.: On the sensitivity of undeformed Arctic sea ice to its vertical salinity profile, Geophys. Res. Lett., 32, L16502, doi:10.1029/2005GL023427, 2005.
Vancoppenolle, M., Fichefet, T., and Goosse, H.: Simulating the mass balance and salinity of Arctic and Antarctic sea ice: II. Sensitivity to salinity processes, Ocean Model., 27, 54–69, 2009a.
Vancoppenolle, M., Fichefet, T., Goosse, H., Bouillon, S., Madec, G., and Maqueda, M. A.: Simulating the mass balance and salinity of Arctic and Antarctic sea ice. 1. Model description and validation, Ocean Model., 27, 33–53, 2009b.
Vancoppenolle, M., Bouillon, S., Fichefet, T., Goosse, H., Lecomte, O., Morales Maqueda, M. A., and Madec, G.: The Louvain-la-Neuve sea ice model, Notes du pole de modélisation, Institut Pierre-Simon Laplace (IPSL), Paris, France, No 31 ISSN No 1288–1619, 2012.
Vancoppenolle, M., Meiner, K. M., Michel, C., Bopp, L., Brabant, F., Carnat, G., Delille, B., Lannuzel, D., Madec, G., Moreau, S., Tison, J.-L., and van der Merwe, P.: Role of sea ice in global biogeochemical cycles: emerging views and challenges, Quaternary Sci. Rev., 79, 207–230, 2013.
Vihma, T.: Effects of Arctic sea ice decline on weather and climate: a review, Surv. Geophys., 35, 1175–1214, 2014.

GMDD
8, 3403–3441, 2015

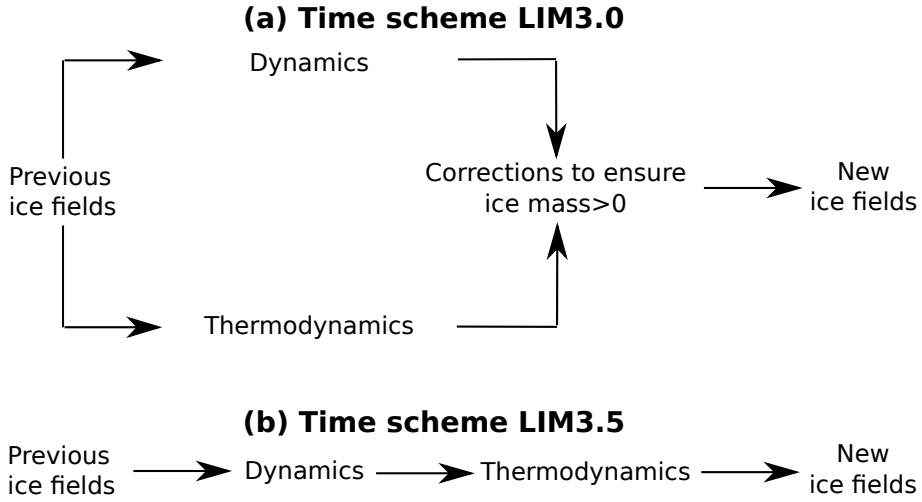

Figure 1. Illustration of the changes in the time stepping scheme. **(a)** The original time stepping scheme used in LIM3.0 treats ice dynamics and thermodynamics in parallel, requiring a correction step to ensure that the ice mass is strictly positive. **(b)** The new time stepping scheme of version 3.5 is sequential, so that dynamics are calculated before thermodynamics, and therefore no correction is needed.

GMDD
8, 3403–3441, 2015

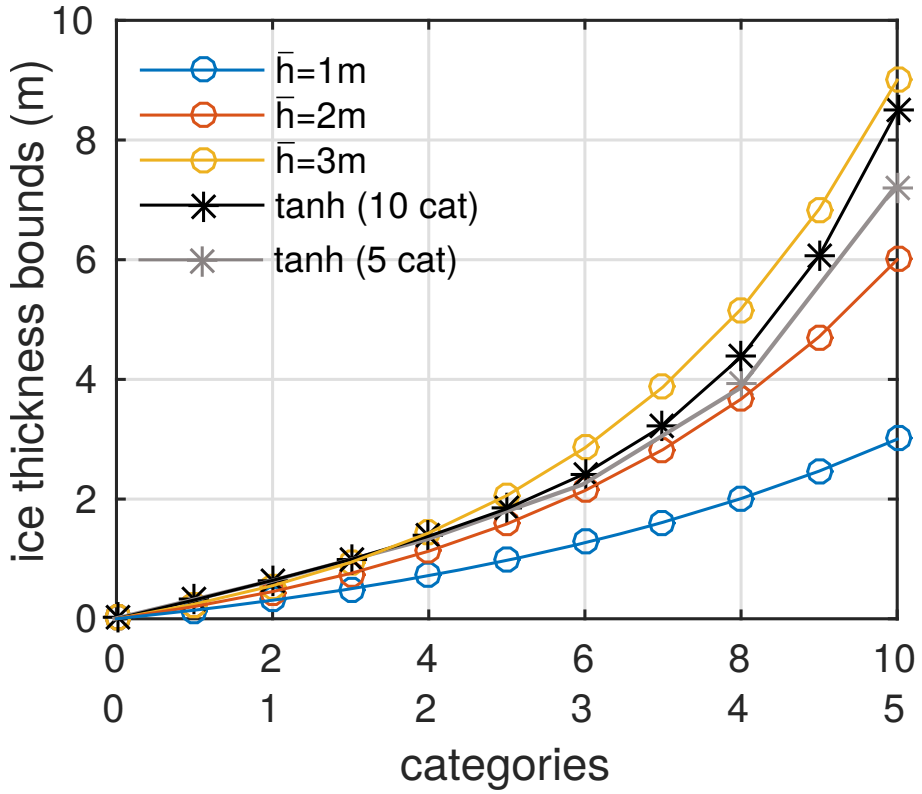

Figure 2. Thickness category boundaries (m) as a function of categories (5 or 10). The tanh formulation from CICE and used in the former version 3.0 of LIM is represented in gray and black for 5 and 10 categories respectively. The formulation used in the new version 3.5 of LIM is proportional to $(1+h)^{-\alpha}$, where $\alpha = 0.05$, and does not depend on the number of categories. It is displayed above for three different mean ice thicknesses $\overline{h}$ (1, 2 and 3 m), $\overline{h} = 2$ m being the closest to the tanh formulation.

GMDD
8, 3403–3441, 2015

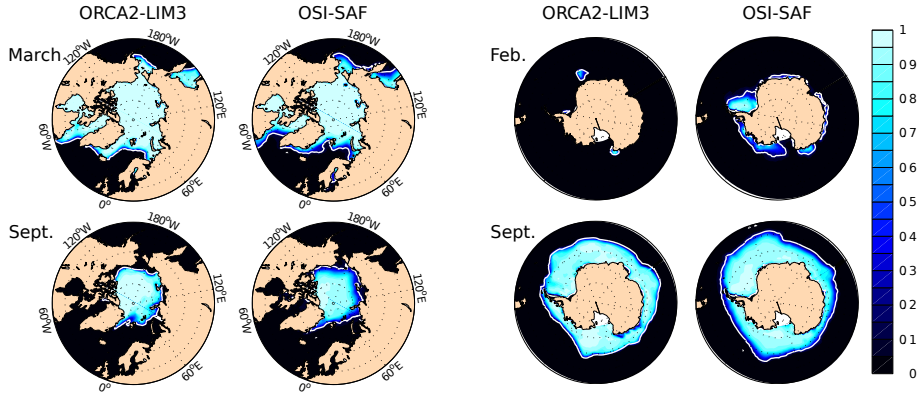

Figure 3. Mean sea ice concentrations from the simulation ORCA2-LIM3 and the observations OSI-SAF for March and September in the Arctic (left panels) and February and September in the Antarctic (right panels). The white line delimits the 15 % ice concentration contour.

GMDD
8, 3403–3441, 2015

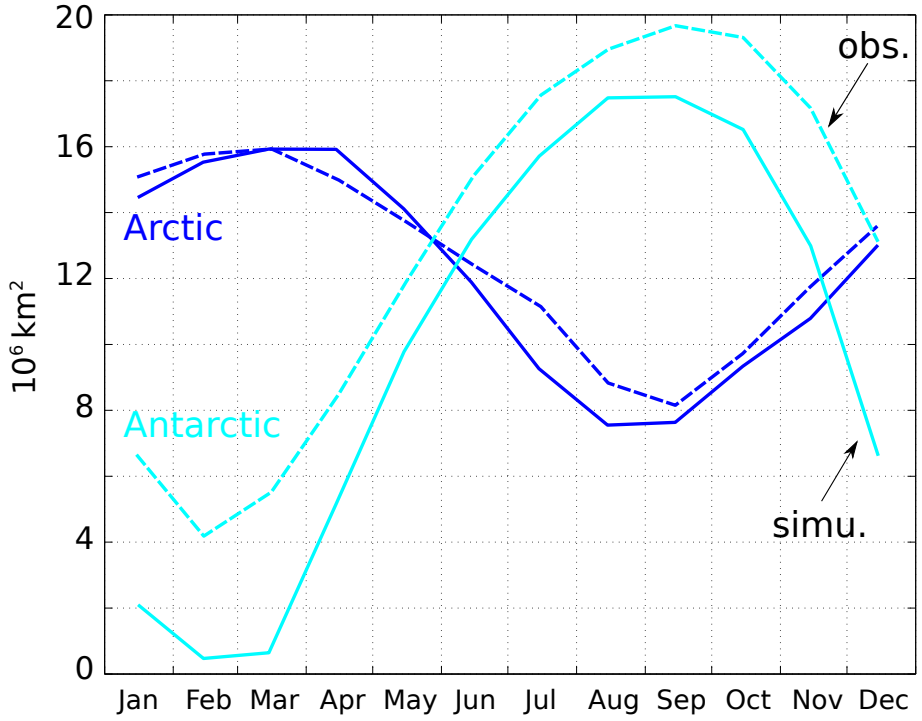

Figure 4. Mean seasonal cycle of sea ice extent (i.e. area inside the 15 % concentration contour) in the Northern (in blue) and Southern (in cyan) Hemispheres from the ORCA2-LIM3 simulation (solid lines) and as derived from OSI-SAF observations (dashed lines). Units are in 10^6 km^2.

GMDD
8, 3403–3441, 2015

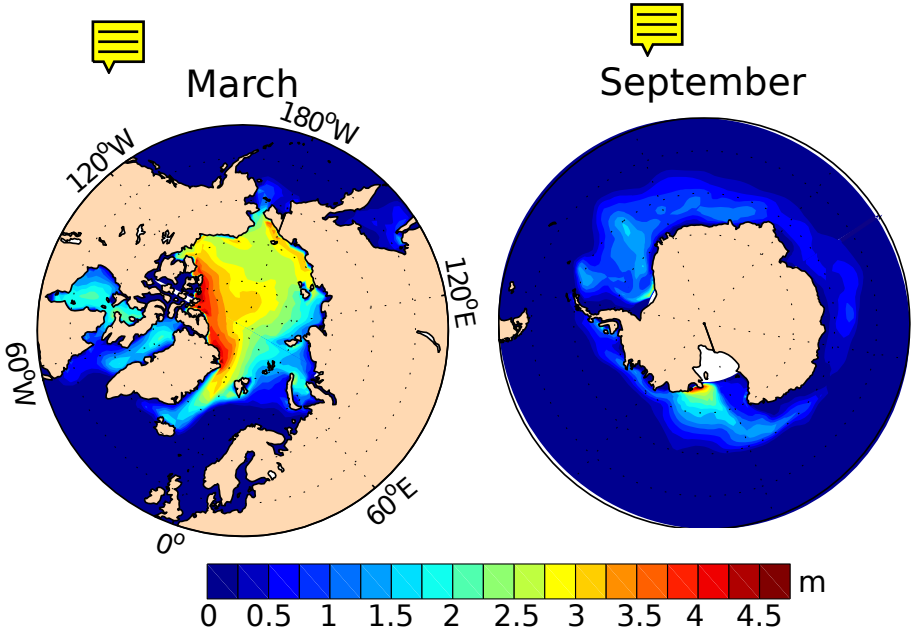

Figure 5. Mean simulated sea ice thicknesses (in m) at the time of the maximum ice volume: for March in the Northern Hemisphere and for September in the Southern Hemisphere.

GMDD
8, 3403–3441, 2015

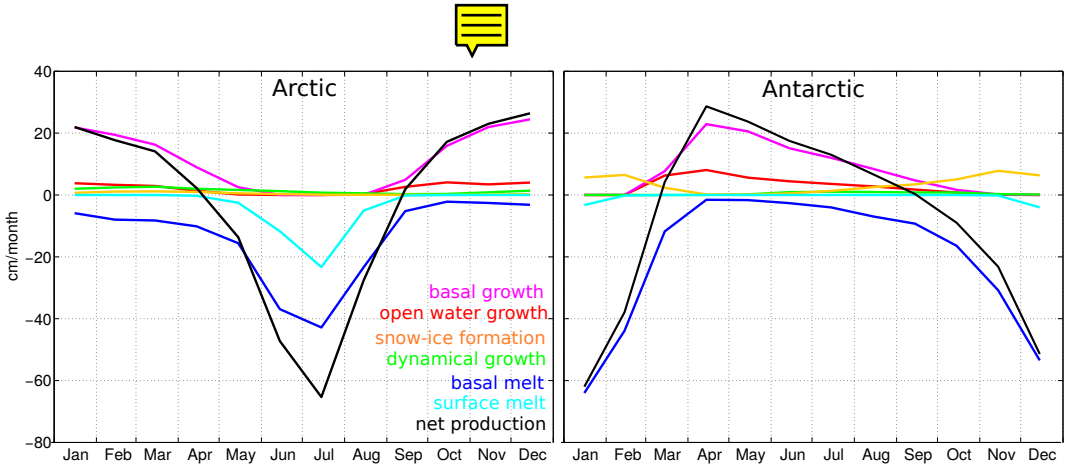

Figure 6. Simulated mean seasonal cycles of the different ice mass balance processes in the ORCA2-LIM3 simulation: Arctic (left panel) and Antarctic (right panel). Ice grows from the base (magenta), in open water (red), by snow–ice formation (orange) or by freezing of sea water trapped in the ridges (green). Ice melts at the base (blue) and surface (cyan). Ice advection is nil here since diagnostics are hemispheric. The black line is the net ice production (i.e. the sum of all the processes). Units are in cm month^{-1}. Positive and negative values represent creation and destruction of sea ice, respectively.

GMDD
8, 3403–3441, 2015

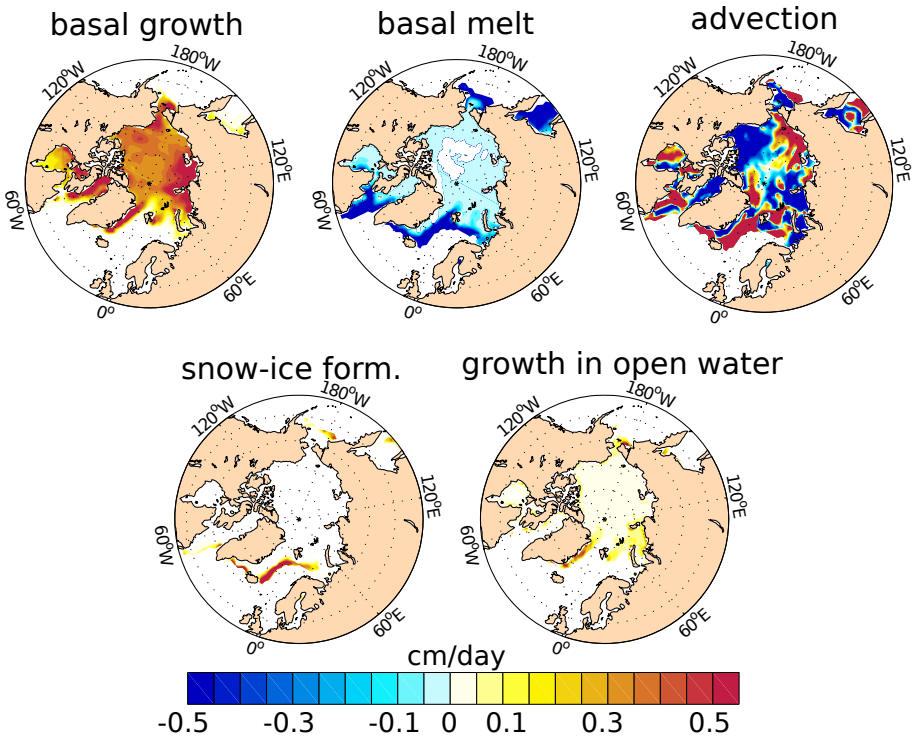

Figure 7. Horizontal distribution of the five relevant processes contributing to the sea ice mass balance in March in the Northern Hemisphere, from the ORCA2-LIM3 simulation. Units are in cm day^{-1}. Positive and negative values represent creation and destruction of sea ice respectively.

GMDD
8, 3403–3441, 2015

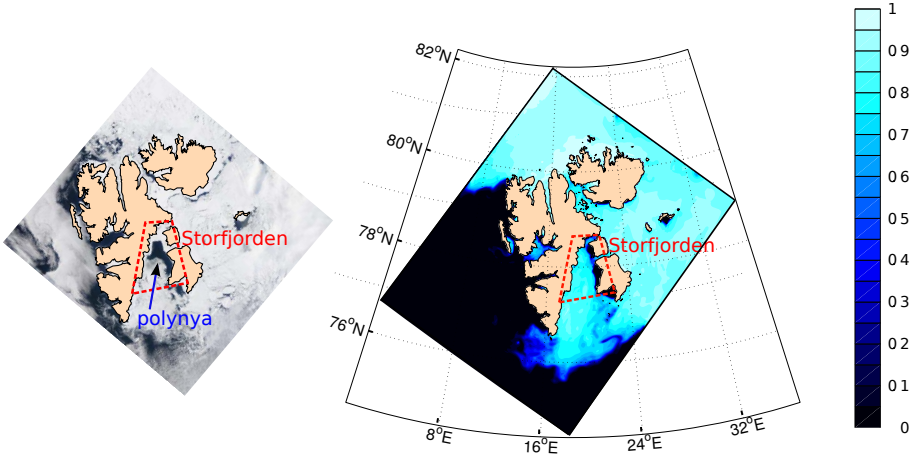

Figure 8. Left panel: satellite MODIS image of the Svalbard Archipelago (22 May 2002). Note that clouds and sea ice are both white. Right panel: 1 day averaged simulated sea ice concentrations at the same date from the high-resolution regional simulation. In both pictures, ice is pushed away from the shore by northeasterly winds, allowing formation of a polynya along the east coast of Storfjorden.

GMDD
8, 3403–3441, 2015

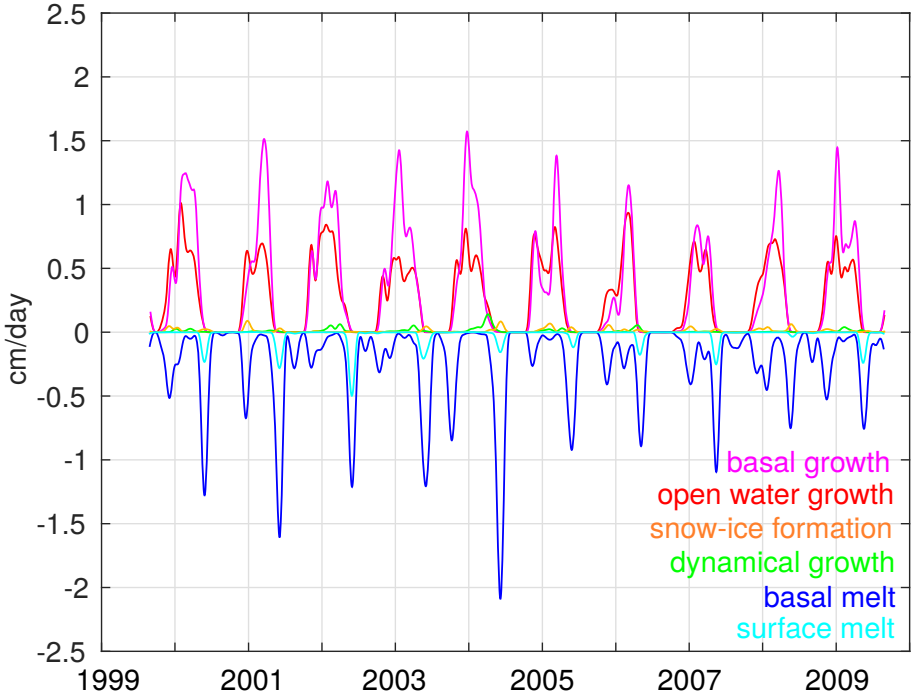

Figure 9. 10 year interannual variability of the processes involved in ice evolution integrated over the Storfjorden area from the regional simulation. Processes are the same as in Fig. 6, plus an advection term corresponding to ice coming in and out of the area which is not shown for more clarity. Units are in cm day^{-1}. Positive and negative values represent creation and destruction of sea ice respectively. Note that for more readability, variations are smoothed with a Hanning filter at a period of 2 months.

GMDD
8, 3403–3441, 2015